RESEARCH ARTICLE

VOLCANICA

The use of UAV-based visible and multispectral thermal infrared data for active volcano monitoring and analysis: test of a low-cost solution applied to the 2022 Meradalir eruption

James O. Thompson*[α], Emanuel Giovanini[β], Kenneth S. Befus[α,γ], Edward W. Marshall[δ], and Chelsea M. Allison[γ]

[α] Jackson School of Geosciences, The University of Texas at Austin, Austin, TX 78712, USA.
[β] Institut für Geochemie und Petrologie, ETH Zürich, 8092 Zürich, Switzerland.
[γ] Geosciences Department, Baylor University, Waco, TX 76798, USA.
[δ] Nordic Volcanological Center, Institute of Earth Sciences, University of Iceland, Reykjavik, Iceland.

Abstract

Timely analysis of active lava flow dynamics and emplacement are typically limited by current ground, UAV, and satellite-based observational capabilities. The Python Miniature Thermal Instrument for Uncrewed Aircraft Systems (PyMTI-UAS) is a relatively inexpensive, low-mass, low-power multispectral thermal infrared instrument capable of measuring rapid changes in thermal and gas dynamics of lava flows to at high resolution. The 2022 Meradalir effusive eruption in Iceland offered an opportunity to acquire visible and multispectral thermal infrared data with PyMTI-UAS of recently emplaced lavas. A successful deployment occurred during the end of the 2022 eruption and the resulting thermal infrared data provide insights into lava surface texture relationships, post-emplacement alteration, and gas and thermal flux during cooling. This study demonstrates that PyMTI-UAS offers the framework to provide accurate multispectral thermal infrared data at low cost from small UAVs to provide data vital for monitoring volcanic activity and aiding hazard response.

Keywords: UAV Multispectral Thermal Infrared Spectroscopy; Visible and Thermal 3D Reconstructions; Lava Morphology; Meradalir, Iceland; Structure From Motion.

Submitted: 2024-03-06 | Accepted: 2025-04-24 | Published: 2025-06-11

Editor: M. James | Typesetter: A. Ryan

1 Introduction

Large lava flows (>5 km^2) are routinely imaged from orbit to investigate eruption rates and lava flow dynamics to improve hazard assessment and response. Such satellite-based remote sensing presents significant limitations associated with spatial resolution (typically >30 m in the thermal infrared (TIR)). In addition, the relatively low saturation temperatures of current TIR instruments make it harder to detect small scale temperature changes both across and down flow from orbit. Increased proximity improves TIR assessments of highly dynamic volcanic surfaces (i.e. lava, gases, and ash), as well as other phenomena like wildland fires, urban heat, and power plant emissions. To that end, we developed a TIR imaging system designed to mount under a small uncrewed aerial vehicle (UAV), which provides an advantage over conventional ground-based cameras by the ability to cover large areas quickly and deploy over inaccessible/dangerous regions. Volcanic hazards are a primary focus of the system, which was intentionally developed to be cost-effective so it could be deployed by agencies and observatories around the world. The UAV-borne TIR imaging system also collects hypertemporal multispectral and fully unsaturated TIR data that enable thermodynamic analyses over timescales of seconds, with implications for lava flow emplacement but also for air quality monitoring, lava modeling, and management efforts.

During effusive eruptions, lava flow emplacement and propagation pose hazards to the surrounding infrastructure and population. In a hazard response scenario, gathering observations (lava temperature, effusion rate, crystal content, vesicle content, local topography) to perform accurate flow modeling is time consuming and can take several days to process [Ramsey and Harris 2013]. Temperature is considered the foremost variable because it influences rheology [Harris et al. 1998; Cashman et al. 1999; Gregg and Fink 2000].The majority of basaltic lava flow propagation models rely on input variables including viscosity, effusion rate, and local topography, where viscosity is influenced by temperature, crystals and vesicles, with temperature being inversely correlated to viscosity [Park and Iversen 1984; Dragoni and Tallarico 1994; Harris and Rowland 2001]. Thermal properties are routinely estimated/assumed from previous field or laboratory studies [e.g. Harris and Rowland 2001; Avolio et al. 2006; Bilotta et al. 2012], or are derived from satellite-based Advanced Very High Resolution Radiometer (AVHRR) and Moderate Resolution Imaging Spectroradiometer (MODIS) thermal infrared (TIR) data [e.g. Del Negro et al. 2007; Vicari et al. 2008; Herault et al. 2009; Vicari et al. 2011]. Near-ground UAV-based observations allow visual observations to be combined with high spatial, spectral, and temporal multispectral TIR data acquisitions, thus allowing active lavas to be monitored with near real-time results.

The characterization and mapping of effusive eruptions, including lava cones, lava flows, and fumaroles (Figure 1) using UAV-based instruments is now a common practice within volcanology [e.g. Carr et al. 2019; James et al. 2020]. Safely accessing such dynamic events on the ground remains challenging, but UAV systems now provide feasible means to ac-

* james.thompson@beg.utexas.edu

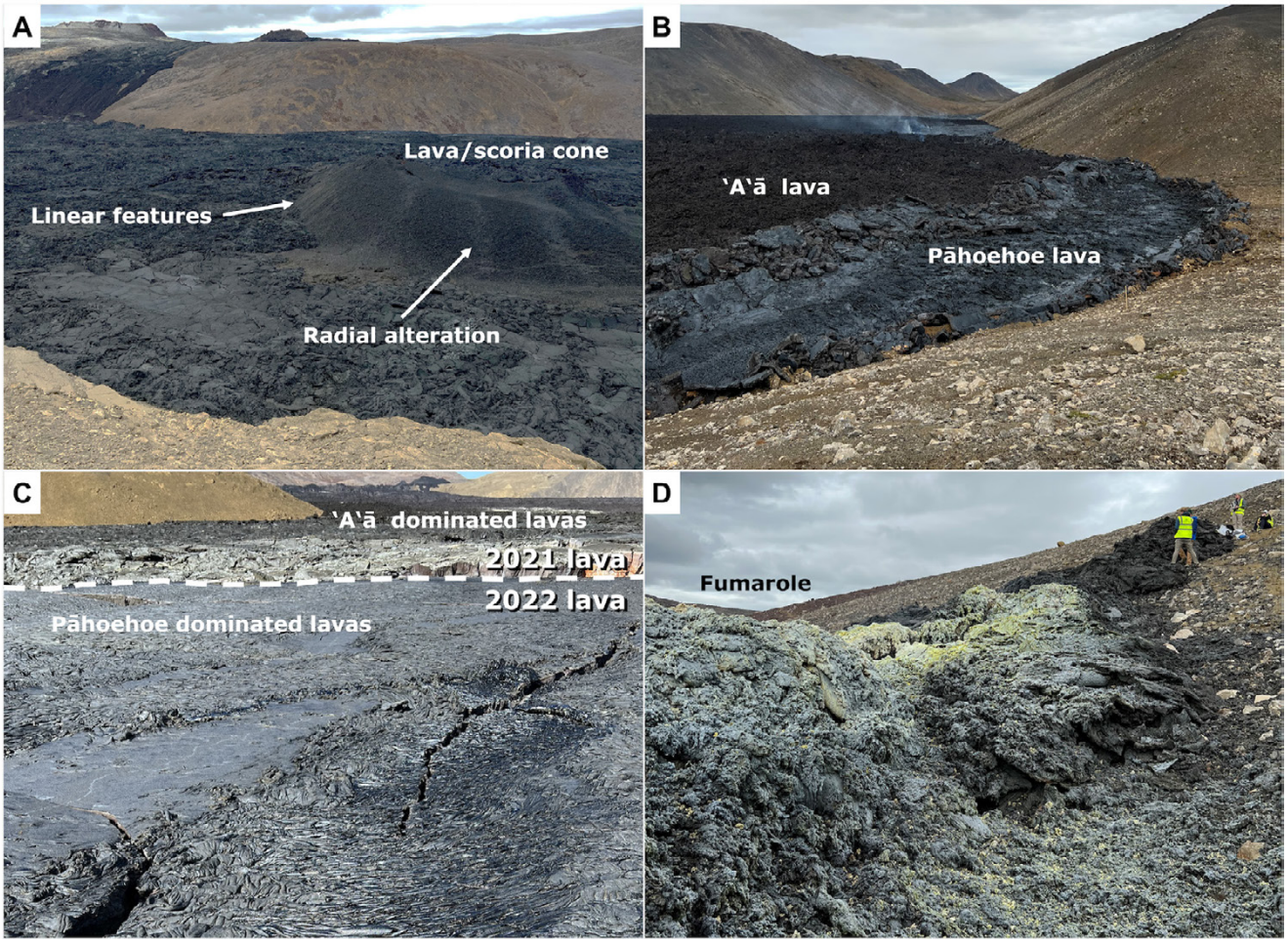

Figure 1: Photos of the Meradalir lava flow field from August 23–26, 2022, highlighting the main regions of interested investigated during the deployment. [A] Lava cone (vent), [B] distal lava flow front to the east, [C] distal lava flow to the south, and [D] an active fumarole near the lava cone [A]. These observations are used to inform our interpretations of the UAS-based results.

quire observations at high spatial, temporal, and spectral resolutions, as well as perform rapid mapping of local sites. UAV systems also offer a more cost-effective means of acquiring these datasets remotely, compared with more expensive and complex crewed aircraft deployments (e.g. airplanes and helicopters). The flexibility of UAV deployments allows targeted measurements of dynamic lava emplacement processes from a safe distance and with some logistical advantages over crewed platforms [Albadra et al. 2020; James et al. 2020]. The majority of previous UAV-based data include visible and broadband thermal infrared datasets that have been used in photogrammetry and/or feature tracking [Carr et al. 2019; Albadra et al. 2020; James et al. 2020; Etchells et al. 2022]. However, UAVs used in volcano research tend to lack the high spatial resolution multispectral data required for detailed thermal/compositional analysis, or are far too expensive (>$100,000) for widespread adoption by global civil service agencies tasked with volcano monitoring. We recognized that a valuable opportunity existed to develop an inexpensive open-access alternative that would be deployable on most low/moderate lift UAVs (e.g. a payload of <1 kg).

Our UAV-based TIR imaging system was first deployed to the field in the spring of 2022, with an effusive basaltic eruption beginning on August 3, 2022 in Fagradalsfjall, on the Reykjanes peninsula, Iceland. This eruption, referred to here as the 2022 Meradalir eruption, emplaced $11 \pm 0.4 \times 10^6$ m^3 of basaltic lava covering 1.28 km^2, with activity ceasing on August 21, 2022. The 18-day long 2022 eruption has a mean output rate of ~7 m^3 s^{-1}, starting with initial effusion rates greater than 30 m^3 s^{-1} followed by an exponential declining effusion rate [Gunnarson et al. 2023; Pedersen et al. 2024]. The 2022 Meradalir eruption occurred proximally to the 2021 Geldingadalir lava field, which emplaced $150 \pm 3 \times 10^6$ m^3 of basaltic lava covering an area of 4.8 km^2 from March 19, 2021 to September 18, 2021 [Kahl et al. 2022; Pedersen et al. 2022; Barsotti et al. 2023; Pedersen et al. 2024]. These events were the first known eruptions in the past 700 years on the peninsula, and have provided the volcano community with an accessible opportunity for investigation by modern analytical instruments and techniques [e.g. Sæmundsson et al. 2020; Kahl et al. 2022; Matthews et al. 2024].

The August 3, 2022, eruption started through a 375 m long effusive fissure northeast of the 2021 eruption centers [Parks et

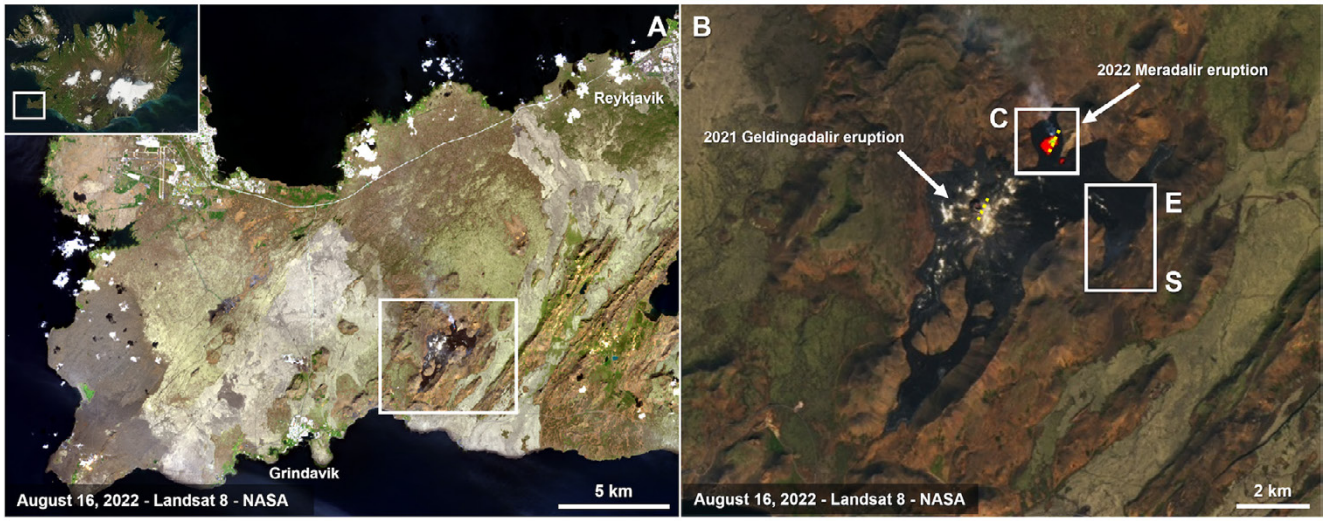

Figure 2: [A] Overview of the lava flow field on the Reykjanes peninsula during the 2021 Geldingadalir and 2022 Meradalir eruptions. [B] The C, E, S labels refer to analyses at the proximal lava/scoria cone (Figure 1A), eastern distal flow front (Figure 1B), and southern distal flow front (Figure 1C), respectively. Note the yellow dotted lines represent the approximate location of the initial fissures of both eruptions.

al. 2023]. Over the subsequent days the activity converged to the north of the fissure forming a centralized vent (Figure 1A, label C in Figure 2B. Lava from the fissure and later from the central vent mainly propagated to the southeast for ~2 km, bounded by preexisting topography [Parks et al. 2023; 2024] (Figure 1B). This vent was active until the end of the effusive eruption on August 21, 2022. Field deployment at Meradalir commenced on August 23, just 2 days after the eruption ceased, when the site was free from tourists and remained an excellent natural volcanic laboratory. The objectives of the 2022 Meradalir eruption deployment were to (1) test the system over a range of eruption features (lava flows, fumaroles), temperatures, and flight conditions to assess the limitations of the system in a near real world eruptive scenario; (2) to understand the complex relationship between lava surface morphology, surface temperature, and post-emplacement conditions, and (3) understand how those relationships relate to vent conditions and post-eruption extents. Here, we share concurrent visual and thermal results of the vent and distal portions of the lava field, and our subsequent interpretations of vent dynamics and emplacement processes.

2 Methods

We developed the Python Miniature Thermal Instrument for Uncrewed Aircraft Systems (PyMTI-UAS; Figure 3) as a multispectral TIR imaging system that can be mounted on a small UAV (i.e. DJI Phantom 3). The design resembles a miniature and refined version of the MMT-Cam, previously developed and successfully deployed on Hawai'i [Thompson et al. 2019; Thompson and Ramsey 2020a; b]. The PyMTI-UAS system was specifically engineered to optimize miniaturization, cost reduction (<$2000 USD), and automation. Here, we make the PyMTI-UAS design freely available* for researchers, especially those at volcano observatories but also across the Earth and environmental sciences, to deploy it as a valuable and low-cost tool. We flew PyMTI-UAS in challenging real-world conditions, above an active volcanic system, in rugged terrane, in winds up to 40 km h^{-1}, and in sporadic precipitation (Figure 3B).

The PyMTI-UAS system uses FLIR Lepton 3.5 commercial, off-the-shelf, uncooled VOx microbolometer thermal imaging detector cores. The Lepton core and microcontroller interface are powered directly from the UAV power source (lithium batteries), resulting in 20–40 minutes of flight time, which varies with atmospheric conditions. The system acquires TIR data at five spectral bands (8.5, 9.0, 10.0, 10.5, and 11.0 μm) with a 160 × 120 active pixel focal plane array [FLIR Systems 2014; 2018]. An instantaneous multispectral image set is captured every 1.0 second. The TIR data are saved locally on the microcontroller and downloaded post flight for calibration and processing. The TIR core has two operating modes that allow it to collect unsaturated TIR data, even over high temperature surfaces (<1600 K). PyMTI-UAS thus provides the resolution required to observe spatiotemporal variability of cooling targets (Figure 3A). The TIR data are then combined with a visual dataset acquired from a second UAV. Our deployment used the DJI Phantom 4 for the PyMTI-UAS and a DJI Mavic 3 for visual observations, with the Phantom 4 visible camera providing backup data at lower resolution compared to the Mavic 3 data. The visible camera on the DJI Mavic 3 has an image sensor format of 4/3 CMOS, with a field of view of 84° and 5280 × 3956 pixel focal plane array.

2.1 Data collection and calibration

Field deployment commenced on August 23, just 2 days after the eruption ceased, and continued until August 26, 2022. During deployment at Fagradalsfjall, the visual data were collected from an altitude of 30 m above ground level over the three observation sites (cone, east distal, and south distal; Fig-

*see GitHub repository; https://github.com/jthompson2710/PyMTI-UAS

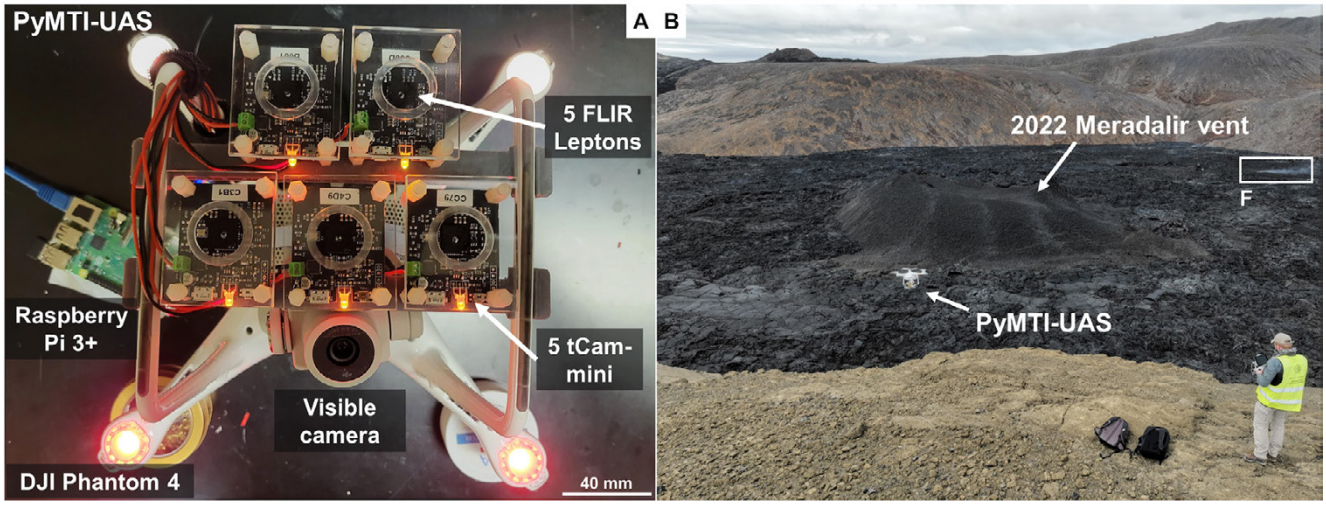

Figure 3: [A] View of the bottom of the PyMTI-UAS showing five FLIR Lepton 3.5 cores shielded by plexiglass squares that hold the TIR bandpass filters. The system is mounted to the base of a DJI Phantom 4 using a custom 3D printed plastic carriage. [B] PyMTI-UAS deployed on the active lava flows at Fagradalsfjall, Iceland in August 2022. Note, [F] shows the location of the multispectral analysis in Figure 10.

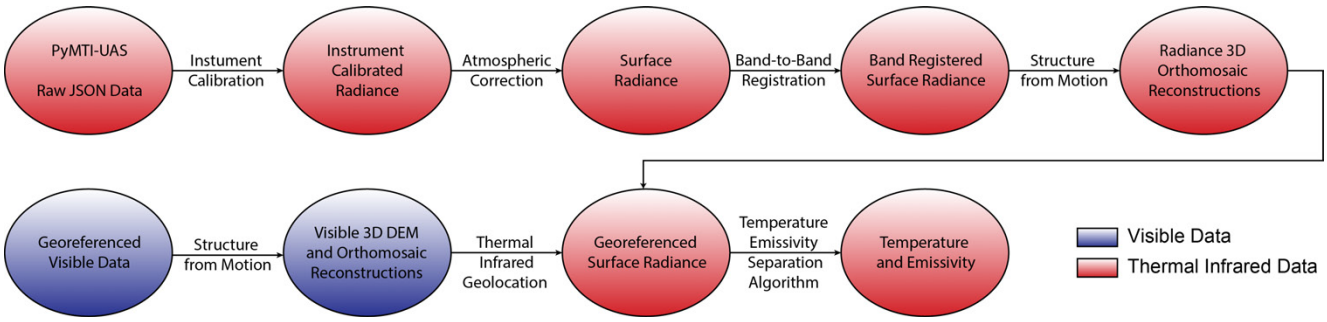

Figure 4: The processing pipeline of the TIR (red ovals) and visible (blue ovals) products.

Table 1: An example of the DEM validation results from cross correlation and control points.

Region	Location (latitude, longitude)	Elevation		
		This study	Gunnarson et al. [2023]	Control point
Cone	63.8985, −22.2490	238.6	237.7	N/A
Cone	63.8980, −22.2491	236.1	236.1	N/A
Cone	63.8976, −22.2480	239.3	238.1	238.5
Eastern Distal	63.8889, −22.2234	185.2	N/A	185.5
Eastern Distal	63.8881, −22.2246	204.7	N/A	204.6
Southern Distal	63.8859, −22.2289	131.9	N/A	131.0
Southern Distal	63.8866, −22.2301	132.8	N/A	133.2
Southern Distal	63.8881, −22.2263	130.7	N/A	131.8

ure 1A, B, C, respectively). The thermal infrared data were acquired from 10–20 m above ground level over the same three observation sites. These flight altitudes were chosen to ensure detailed observations of thermal, textural, and gas variability across the lava flow field at a spatial resolution of <0.15 m. Flights paths were chosen based on: (1) limited duration of flight (~20 minutes), (2) weather conditions (wind speed and direction), (3) access to lava flow field, and (4) target of interest (cone, fumaroles, textures). Flight path planning prioritized limiting the likelihood of vehicle loss. Additionally, during the planning, flight paths that provided ~65 % data overlap were created based on the PyMTI-UAS field of view of 8–22 m and a temporal resolution of 1 Hz.

Raw PyMTI-UAS data were calibrated to correct for instrument geometry (including sensor planarity), optical attenuation, and atmospheric effects. We used variable, full-aperture

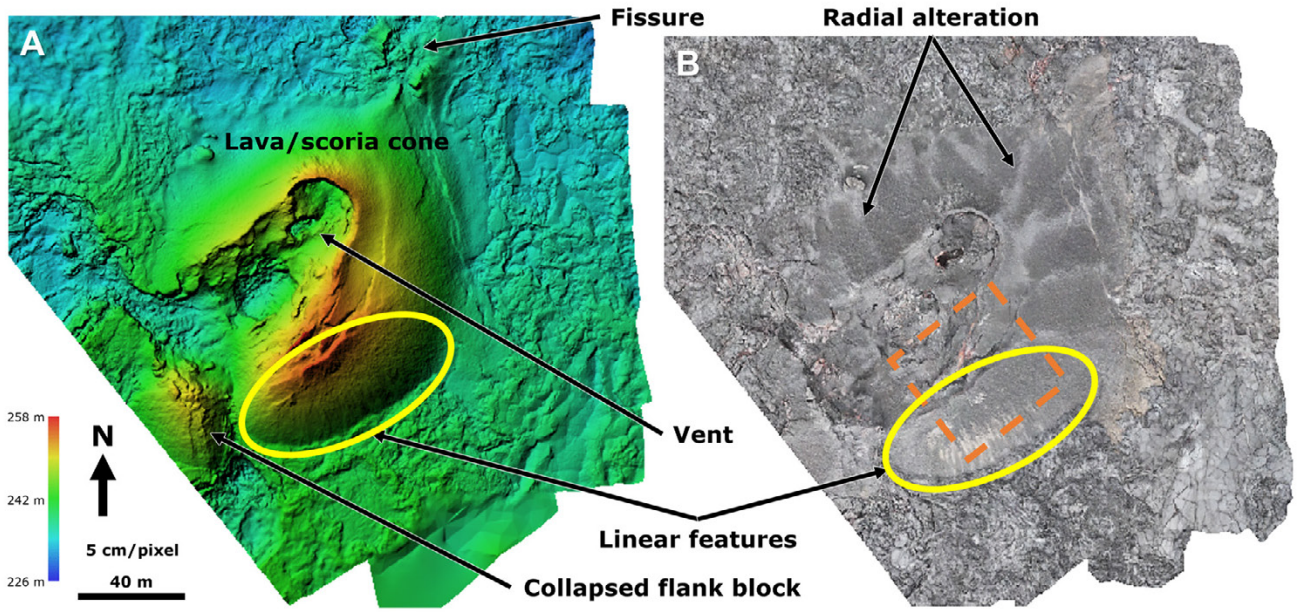

Figure 5: [A] Hill-shaded DEM and [B] orthomosaic reconstructions of the vent during the 2022 Meradalir eruption. The DEM highlights the relief of the vent, collapsed flank block, and linear features. The orthomosaic highlights thermochemical alterations post tephra and lava emplacement.

blackbodies from 283 to 483 K to quantify the instrument response using known target temperatures and internal instrument temperatures. These internal and target temperature corrections account for instrument heating and detector drift [Thompson et al. 2019]. For example, over active (hotter; >1000 K) degassing lava flows, the optical attenuation will increase with temperature of the sensor and optics, causing self-reflective effects and response shift. Instrument geometry correction or sensor planarity was achieved through calculating optical distortion coefficients based on a template matching algorithm in the laboratory [Zhang 2000; Liu et al. 2023]. Thermal data of a metallic "checkerboard" pattern target with a temperature contrast achieved by heating from sunlight were used for the matching, with distortion coefficients calculated using OpenCV. This method was chosen based on the mean reprojection error analysis conducted in previous studies [e.g. Liu et al. 2023; Roshan et al. 2024]. The distortion coefficients were then applied to at-sensor radiance data to correct for sensor planarity.

To convert the at-sensor radiance data to surface radiance data, an atmospheric compensation technique was developed that is reliant upon temperature, humidity, and line-of-sight distance [e.g. Rothman et al. 2013; Thompson et al. 2019] (Figure 4). For example, volcanic gases absorb radiation at certain wavelengths, causing the lava surface to appear cooler than the true value. Briefly, the PyMTI-UAS data calibration uses a modified Temperature-Emissivity Separation (TES) algorithm to separate emissivity and temperature from the atmospherically corrected surface radiance data and account for spectral contract across different wavelengths [e.g. Gillespie et al. 1996; Thompson et al. 2019]. Cumulative errors in PyMTI-UAS data are <4 % based on the thorough calibration procedure.

2.2 DEM and orthomosaic generation

Overlapping flight paths produced visible camera image overlap of 50–80 %, with a ground sampling distance of ~14 mm (Figure 4). We aligned the images in Metashape and generated Digital Elevation Models (DEMs) of the proximal vent and distal flow fronts. Dense point clouds were produced by processing at the "high quality" and "mild depth filtering" parameter settings in Metashape to preserve the small details. After the point clouds were reconstructed, polygonal mesh models were generated at the "high" polygon count and interpretation parameter settings in Metashape. DEMs were produced from the dense point cloud models. Visible orthomosaics with a 50 mm pixel size were then generated using the DEMs. The visible data products were georeferenced using the onboard GNSS data (corrected by ground control station), resulting in a georeference accuracy of <2 m horizontally and ~3 m vertically. The DEMs and visible orthomosaics were validated for accuracy using a combination of comparison with previously published DEMs and ground control points. All elevations validated were within 1.5 m of the verification data, with a mean error of 0.65 m (Table 1).

Thermal 3D orthomosaic surface models were also produced. Thermal data were collected with an image overlap of 40–75 %, with a ground sampling distance of 30–50 mm (Figure 4). The calibrated and atmospherically corrected radiance, temperature, and emissivity data were spatially aligned between bands (band-to-band) and georeferenced across the deployment area. The band-to-band registration was achieved by implementing a Discrete Fourier Transform technique for translation, rotation and scale-invariance between band images [e.g. Reddy and Chatterji 1996; Xie et al. 2003; Matungka et al. 2008]. The algorithm was implemented by transla-

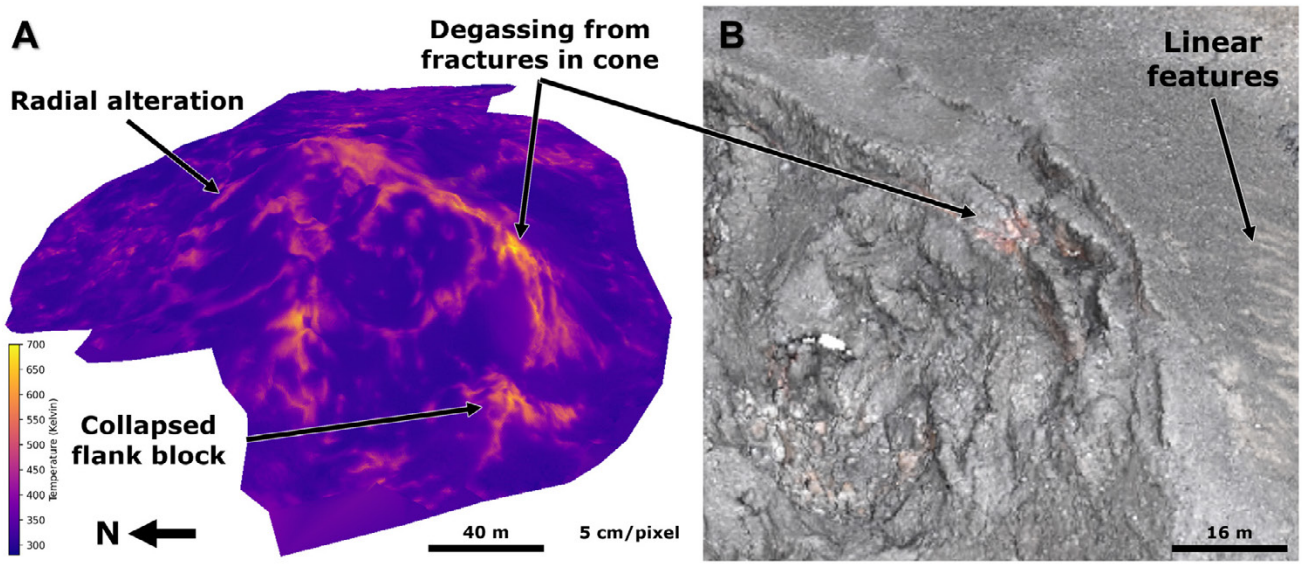

Figure 6: 3D [A] thermal and [B] zoomed visual orthomosaic (from orange box in Figure 5B) reconstructions of the vent during the 2022 Meradalir eruption. The thermal mosaic illustrates the thermal flux pathways post emplacement. The visual orthomosaic highlights interpreted thermochemical alterations and degassing post emplacement. Note the oblique view and orientation change of the reconstructions, to highlight the structure of the thermal variability and interpreted alteration.

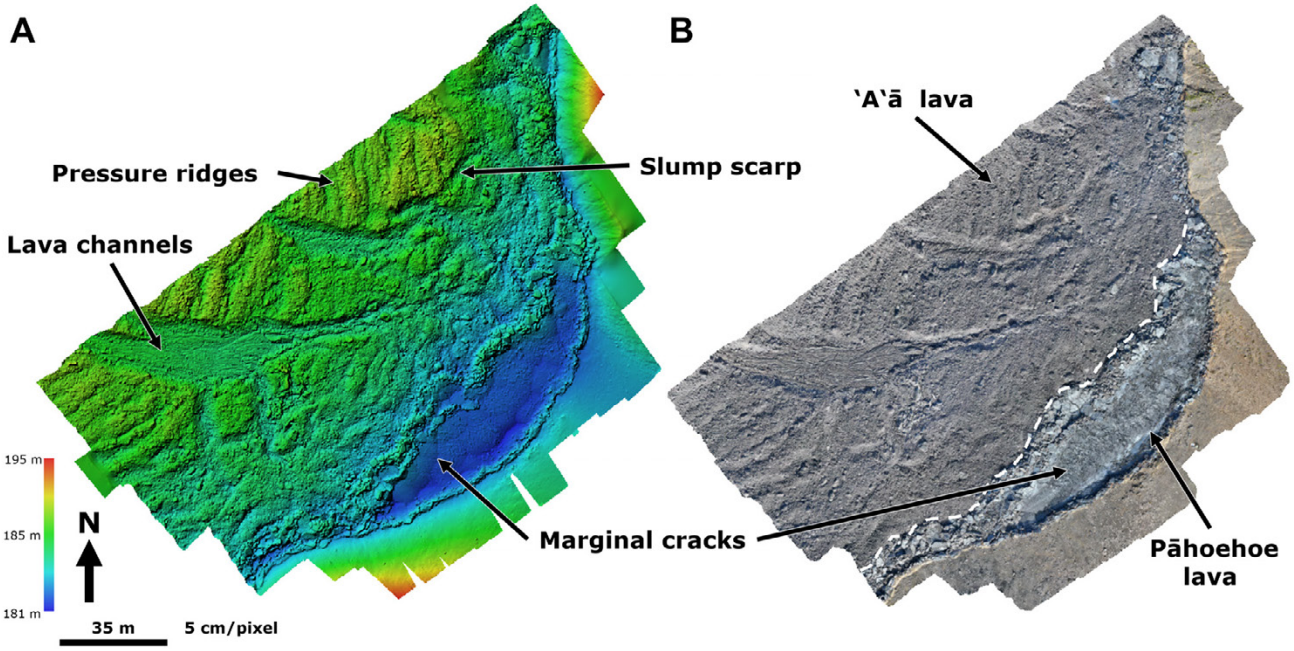

Figure 7: 3D visual reconstructions of the eastern distal lava flow front emplaced during the 2022 Meradalir eruption: [A] hillshaded DEM and [B] orthomosaic reconstructions. The DEM highlights relief, pressure ridges and inflation-related marginal cracks planes, channels, slump scarps (vertical offset), and surface morphology. The dashed white line provides our interpretation of the boundary between lava textures related to re-emplacement of remnant mobile 2021 lavas in response to the overlying 2022 lava (based on Hennig [2023]).

tion, rotation, and scale variation calculations between two bands, and by calculating the image spectrum using the log-polar transformation. The technique was applied to all the bands based on the same reference band (8.5 µm) and optimized to remove any residual geospatial offsets. The maximum spatial errors are 0.15 × 0.16 pixels (in x and y, typically at the image corners), resulting in approximately 10–50 mm spatial inter-band registration error during the deployments in Iceland. The individual band-to-band registered TIR images were then photogrammetrically processed using Structure from Motion (`Agisoft Metashape Professional 2.1`) to complete the thermal 3D surface model. The georeferenced visible 3D structures were overlain on the TIR datasets to produce georeferenced TIR datasets, with an accuracy within 3 m.

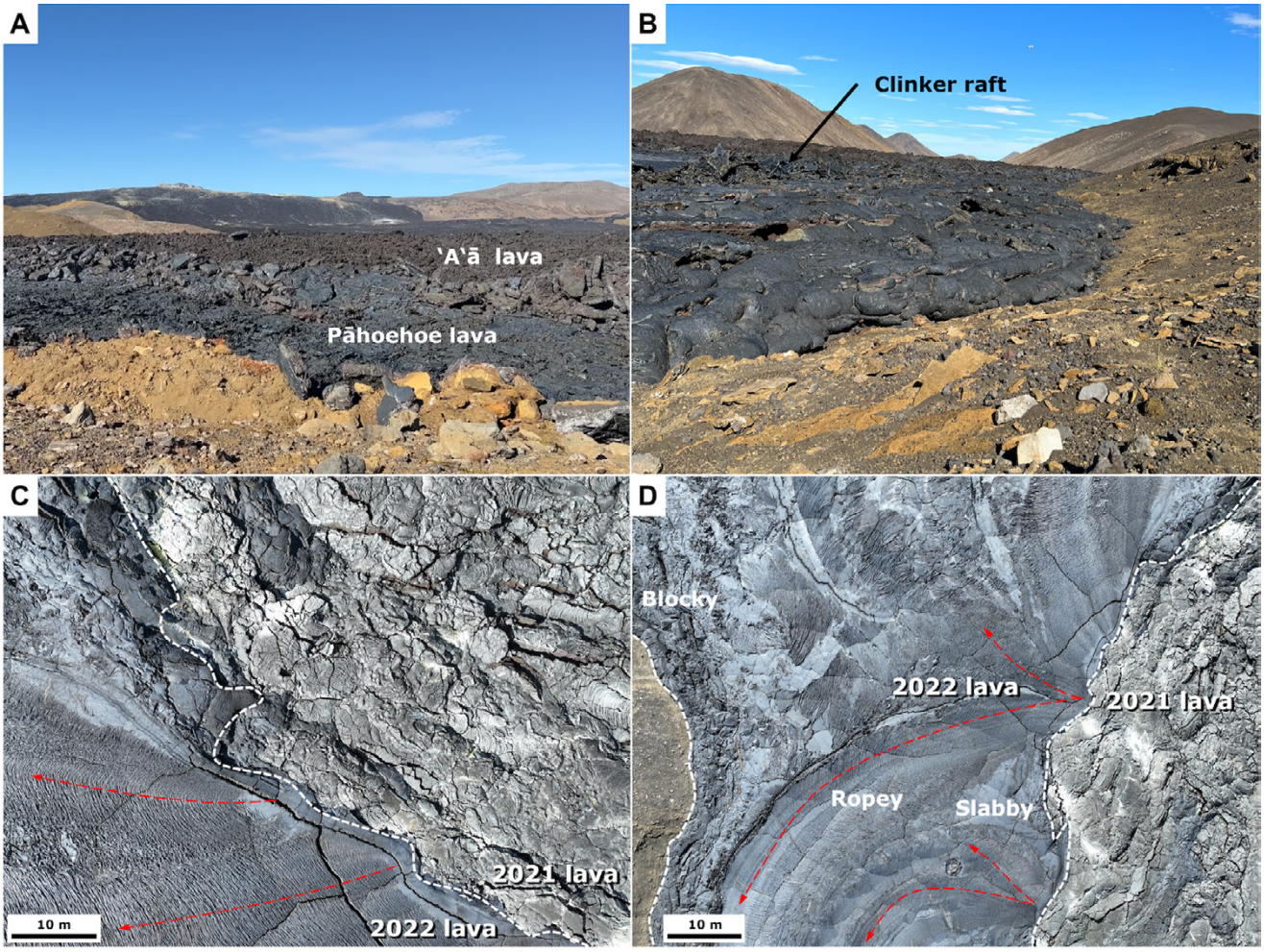

Figure 8: Photos of the Meradalir lava flow field from August 23-26, 2022. [A] distal lava flow front to the east and [B-D] distal lava flow to the south, showing the relationship between flow episodes and lava textures. [C] and [D] were acquired from 63.886425°N, 22.230594°W (166 m altitude) and 63.886262°N, 22.229953°W (227 m altitude). The dashed red arrows indicate potential flow paths (see Volcanology and Natural Hazards Research Group [2022]).

3 Results

3.1 Proximal scoria cone

The DEM reconstructions of the vent region from the PyMTI-UAS deployment reveal the relief of the lava/scoria cone to be ~30 meters and show a collapsed flank block to the southwest, in the orientation of the initial fissure(Figure 5). The collapsed block likely formed when lava breached the flank of the cone, similar to those observed at other cones [e.g. Pulido and Riggs 2013]. The DEM and orthomosaic reconstructions also reveal a concentration of ~10–15 linear features to the south of the cone rim, ranging from 4 to 22 m long. The orthomosaic reconstruction highlights lighter units expanding radially 20 to 40 m from the vent across the flanks of the cone (Figure 5), interpreted as low levels of alteration (Figure 1A).

The 3D thermal reconstructions of the vent region show linear elevated thermal features (~500–550 K) expanding radially from the vent that geographically correspond with the lighter domains observed in the visible orthomosaic reconstructions (Figure 5 and Figure 6) and were confirmed in field photos (Figure 1A). There is a pronounced absence of elevated temperatures directly over the vent (<450 K). Instead, elevated thermal anomalies are concentrated at the rim of the lava/scoria cone, along topographic highs (550–700 K). The interpreted high levels of alteration (orange-red deposits; Figure 6B observed in the visible orthomosaic reconstructions correspond to the highest detected thermal anomalies (<700 K) (Figure 6). Elevated thermal anomalies are also observed along the collapsed flank block on the southwest of the vent.

3.2 Eastern distal flow front

The terminal flow front to the east of the vent (label E in Figure 2B) is dominated by block and rubbly surface textures, based on DEM and orthomosaic reconstructions, which are consistent with an ʻaʻā lava morphology (Figure 7). The extreme eastern extent of the flow appears dominated by slabby and ropy pāhoehoe morphology, which is confirmed through field observations and photographs (e.g. Figure 1B and Figure 8A). This region is 30 by 140 m in size, and rests ~10 m topographically below the ʻaʻā. The visible orthomosaic re-

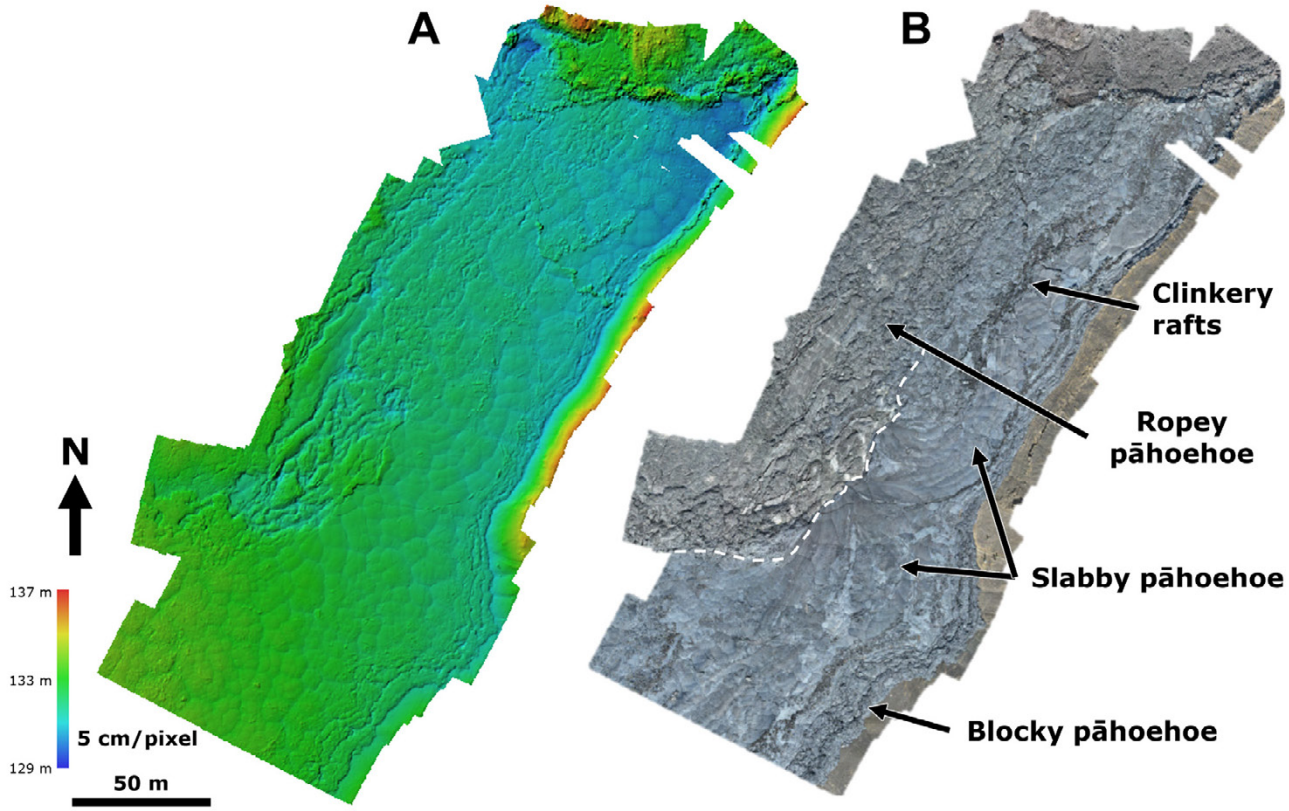

Figure 9: 3D visual reconstructions of the southern distal flow front emplaced during the 2022 Meradalir eruption: [A] hillshaded DEM and [B] orthomosaic reconstructions. The dashed white line provides our interpretation of the boundary between lava textures in the visible orthomosaic (based on Hennig [2023]). The clinker rafts are also shown in Figure 8B.

construction shows an apparent hue difference between these two textures. The DEM reconstruction indicates lava channels ~5–27 m wide running perpendicular to the flow front and pressure ridges that form parallel to the flow front with vertical relief <5 m (from DEM). Channel widths based on the visible orthomosaic agree with the DEM-based estimates to within 0.55 meters and channel depths based on control points agree with the DEM-based estimates to within 0.78 meters.

3.3 Southern distal flow front

The terminal flow front to the southeast of the vent (label S in Figure 2B) is dominated by smooth plate surface textures, based on DEM and orthomosaic reconstructions, which are consistent with pāhoehoe lava morphologies (Figure 8B–D and Figure 9). The visible orthomosaic reconstruction shows a contrast between the ropey-dominated (to the northwest) and slabby-dominated (to the southeast) pāhoehoe lava textures (Figure 9B), as well as lava clinker rafts within the slabby-dominated pāhoehoe lavas (Figure 8B). The DEM reconstruction provides an opportunity to measure the size of the slabby pāhoehoe sheets, which range between 5 and 15 meters in diameter (longer axis) with an average of 9 m. Additionally, the slabby texture transitions to a blockier texture within the final 10 m of the flow front. The blocky texture preserves a rough topography of a collisional jumble of plates as the flow was constrained by the preexisting topography of the valley (Figure 8D).

3.4 Spectral analysis

Spectral analysis from the emissivity data derived from the PyMTI-UAS radiance data (Section 2.1) of the main vent area is able to differentiate between different surface textures, oxidations states, and emissions (Figure 10). The PyMTI-UAS emissivity spectra reveal the presence of high temperature (<690 K) fumaroles emitting SO_2 and water vapor (red and orange spectra in Figure 10), depicted by the strong absorption (emissivity <0.75) at 8.5 and 9.0 μm. Low level surface oxidation is also observed on the cooling flanks (~400–500 K), portrayed a weaker absorption (emissivity >0.8) at 8.5 and 9.0 μm and minimal absorption (emissivity >0.97) at 10 μm (green spectrum in Figure 10). The spectrum acquired of the cooling flank is likely influenced by low concentrations of SO_2. The main lava/scoria cone and its crater are some of the coolest portions of the main vent area. Most areas are <350 K and have a typical basaltic emissivity spectrum, characterized by weak absorption (emissivity >0.89) at all wavelengths (8–14 μm) with a minimum at ~10 μm [Thompson et al. 2019; Thompson and Ramsey 2020a; Biren et al. 2022] (blue spectrum in Figure 10).

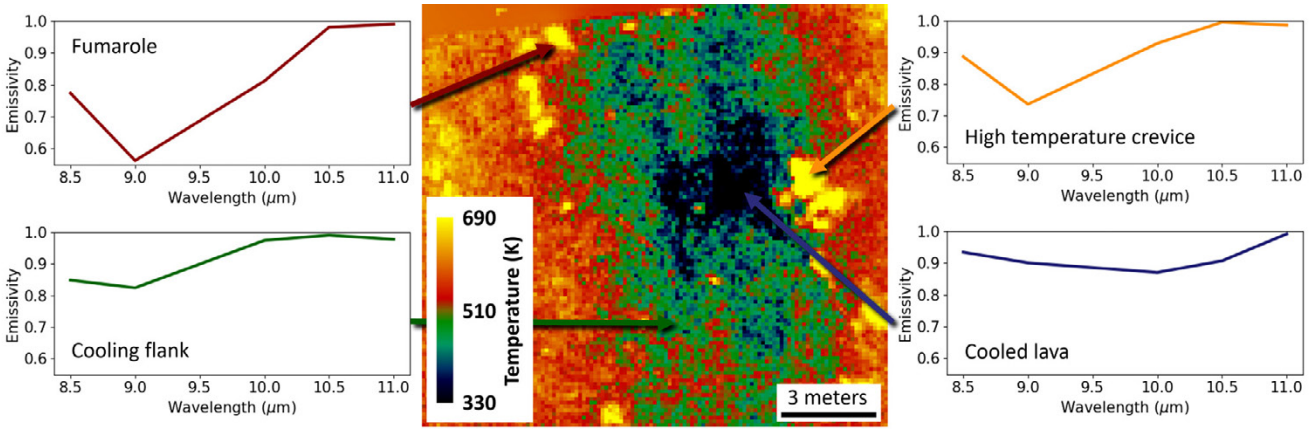

Figure 10: Temperature and emissivity variability across a small active fumarole(~15 × 8 m), shown as inset F in Figure 3B. The processed PyMTI-UAS data can detect SO_2, surface composition (basaltic to felsic), and silica oxidation during surface cooling.

4 Discussion

UAV systems like PyMTI-UAS provide flexible platforms for researchers to acquire accurate, high-resolution visible and TIR data. Such systems allow near real-time monitoring of mass and flux rates of lava and volcanic gases. Multispectral TIR data of volcanoes deliver critical information about thermal and gas fluxes pre-, syn-, and post- eruptions, which are useful for simulations of volcanic products (e.g. lava flows), air quality, and mitigation strategies [e.g. Tang et al. 2020; de-Graffenried et al. 2021; Lowenstern et al. 2022; Barsotti et al. 2023]. Typically, these data are not available in a timely manner and with high resolution (<5 m), limiting the ability to provide detailed analyses and conclusions about activity. This is because of the long repeat cadences of satellite data and limited perspectives offered by ground-based data [Ramsey et al. 2022]. UAV-based TIR instruments provide flexibility and relative logical ease to acquire data at high resolution over entire lava flow fields [Carr et al. 2019; James et al. 2020]. UAV collected data can also be used to produce 3D reconstructions of high resolution DEMs and orthomosaics, which enable the interpretation of emplacement dynamics and surface textures [e.g. Carr et al. 2019; Andaru et al. 2021; Carr et al. 2021].

PyMTI-UAS successfully collected multispectral TIR datasets during the initial field deployment to Fagradalsfjall in August 2022. The data PyMTI-UAS collected in its maiden deployment also offer insights into lava dynamics and cessation-adjacent post emplacement processes, including degassing, surface oxidation, and collapse in basaltic eruptions. Observations show unmodified tephra deposits arranged around the vent, that are aligned with the primary fissure (Figure 11). Such features are typical of Icelandic lava/scoria cones [Boreham et al. 2018]. The relative completeness of the collapsed flank block to the south observed in the DEM, recognizable in both thermal and orthomosaics reconstructions (Figure 5, Figure 6 and Figure 11), implies that the collapse occurred towards the conclusion of the eruption. The development of the cone was observed gradually throughout the eruption with a collapse towards the end of the active eruption from August 12–16, 2022 [Global Volcanism Program 2022]. The data acquired by our study could potentially be collected by other UAS but not with the same thermal infrared spectral information and at the cost achievable through the PyMTI-UAS system.

The thermal features correspond to geomorphological features observed in the DEM and orthomosaics reconstructions. The highest thermal anomalies (<700 K) are observed where the strongest fumarolic/degassing activity occurs on the rim of the lava/scoria cone [e.g. Spampinato et al. 2011]. The interpreted alteration of tephra on the flanks of the cone (observed as lighter linear features on the flanks in Figure 1, Figure 5 and Figure 6), correspond with higher thermal emission regions (<550 K). The alteration implies the thermal perturbations are driven by gas/fluid release patterns post-eruption [Head and Wilson 1989]. Similar radial rill structures have been recognized at active lava domes [Hutchison et al. 2013], eroded cones [Valentine et al. 2007], and altered historic cones [Reynolds et al. 2015; Kósik et al. 2016; Fitch and Fagents 2020]. However, to our knowledge, these radial rill thermal structures have not been previously described at recently emplaced lava/scoria cones. Calvari and Pinkerton [2004] observed similar thermal arcuate cracks on a small portion of the flank of Laghetto cone in 2001, but these were not continuous around the cone, and it is unclear if alteration was associated. The radial rills at Laghetto cone formed as the result of drainage of underlying magma from the fissure causing instability [Calvari and Pinkerton 2004]. If the features on the Meradalir lava/scoria cone are formed by a similar process, it would imply the fissure system is centered directly under the cone, forming the radial rills/cracks around the entire flanks of the cone. Contrary to the Laghetto scoria cone [Calvari and Pinkerton 2004], there are no visible cracks observed in these regions at Meradalir. Additionally, the features at Meradalir formed rapidly in the 1–2 days following the extrusive eruption, which suggests the drainage occurred over a shorter period than at Laghetto. Therefore, we instead propose that the strong radial symmetry, visible alteration, and elevated temperatures suggest these are cooling pathways controlled by rapid (1–2 days) systematic drainage of unerupted magma post eruption.

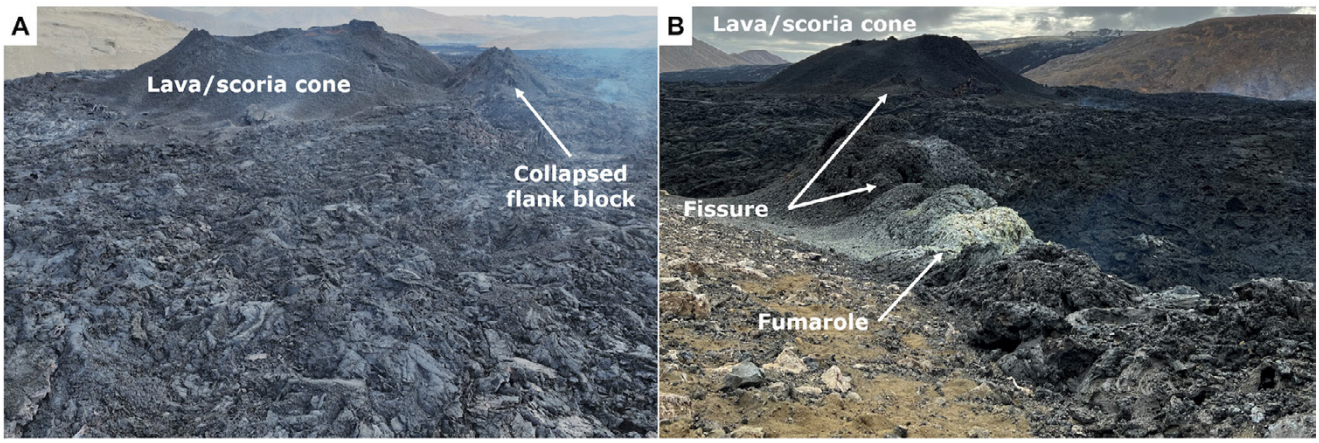

Figure 11: Photos of the Meradalir lava flow field from August 23–26, 2022. [A] lava/scoria cone showing the collapsed flank block, [B] lava/scoria cone showing the relationship between the cone and fissure.

The lava flows produced from the lava/scoria cone breached the southern flank from the base [Global Volcanism Program 2022], resulting in instability and subsequent collapse toward the end of the eruption, due to lava drainage and magma static pressure drop of the magma column. Data acquired by this study show the lava flows around the vent are dominated by blocky and clinker ʻaʻā textures implying the effusion of a relative high viscosity lava potentially emplaced at moderate effusion rates [Harris et al. 2016; Global Volcanism Program 2022] (Figure 1, Figure 5 and Figure 11). Viscosity modeling results imply 2.8–3.5 Pa s at 1665 K compared to 20.9–29.5 Pa s at 1471 K [Soldati et al. 2024]. The deformation modeling results by Parks et al. [2023] measured initial mean effusion rates of 32 m^3 s^{-1} which decreased to ~10 m^3 s^{-1} towards the end of the eruption [Gunnarson et al. 2023]. Therefore, the lavas around the cone were likely emplaced during the later phase, with regions of slabby and ropy pāhoehoe lava inferring some sporadic pooling and inflation of lava during emplacement.

ʻAʻā and pāhoehoe lava are both observed by this study at the distal lava flow fronts (Figure 1, Figure 7, Figure 8 and Figure 9). The main portion of the eastern distal lava flow front is dominated by blocky ʻaʻā textures with large pressure ridges (1–10 m periods and 5–15 m amplitudes). The pressure ridges are attributed to the constriction of the lava flow to the preexisting topography of the valley and typically run perpendicular to the topographic gradient (as shown in Figure 7) [Harris et al. 2016]. A zone of pāhoehoe lava is also observed by this study at the very edge of the eastern distal lava flow front and continues to the southernmost part of Meradalir, appearing much fresher than adjacent 2021 lava (Figure 8). The lava was clearly recently emplaced, as parts of the flow were still hot enough to boil water on the lava surface (>375 K) (see multispectral thermal infrared data in Figure 6A and Figure 10), and the glassy exterior of the lava had not yet been tarnished like the older 2021 pāhoehoe (Figure 8). Although not observed directly, it is hypothesized that this pāhoehoe lens represents a remnant from the 2021 eruption that was remobilized and emplaced in 2022 as a result of the load exerted by the new overlying lava. Other studies also hypothesize this mechanism because the crystal cargo contains large euhedral olivine, which is characteristic of the 2021 lava and not the 2022 lava [Halldórsson et al. 2022; Marshall et al. 2023; Caracciolo et al. 2024; Marshall et al. 2024]. The pāhoehoe texture of this lava observed in this study, implies that these were emplaced through slow toes breakout and inflation dynamics [Harris et al. 2016; Volcanology and Natural Hazards Research Group 2022] (Figure 8). The mineralogical/geochemistry differences from the 2022 lava [Marshall et al. 2023; 2024; Wainman et al. 2024], the emanation of the lava from beneath the 2021 lava, detailed mapping of the interaction between lavas [Barsotti et al. 2023; Hennig 2023] additionally highlighted in this study), and the freshness of the pāhoehoe surface observed in this study (Figure 8), together implies that this lava is remobilized 2021 lava. Work, published only on social media by the University of Iceland, Volcanology and Natural Hazards Research Group [2022] also shows that the new flows raise the surface of the lava field by about 4 m above the level of the pre-2022 eruption lava field, and that the older 2021 lava in the northern extent of eastern Meradalir had inflated. Together, these combined observations infer that beneath the surface of the solidified 2021 lava, molten lava remained and was displaced by the weight of the 2022 lava on the surface of the 2021 lava field, resulting in changes in the height of the lava field and the "squeezing out" of remnant 2021 lava onto the surface.

The extensive (150 × 500 m), low relief (~2 m), and relatively thin (<10 m thick) lava surface in the southern distal region, imply these are slabby pāhoehoe flows that were later inflated [Thordarson and Self 1998; Harris et al. 2016]. The surface is also marked with shallow (~2 m) monoclines and tumuli, features typically associated with thick pāhoehoe flow (e.g. Hawaiʻi). These slabby pāhoehoe flows exhibit distinctive jointing in hexagonal/polygonal structures caused through inflation and contraction of the lava surface. This is consistent with results from Discrete Fourier Transform 2D analysis of the DEM reconstruction, which shows strong (amplitudes >700) variability in 4 orientations (approx. N–S, E–W, NE–SW, and NW–SE) at ~28-m intervals (Figure 12). Similar polygons are present on the pāhoehoe flows from the 1974 Mauna Ulu flows and earlier 1990 Puʻu ʻŌʻō flows [Harris et

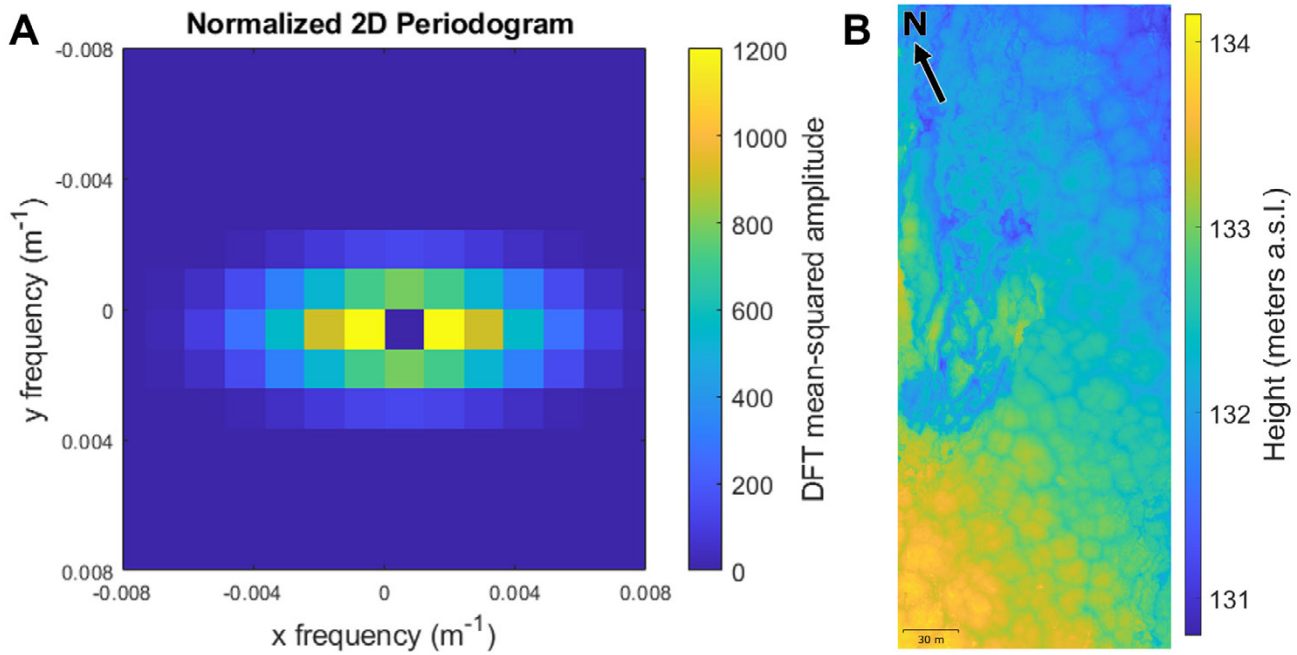

Figure 12: [A] Discrete Fourier Transform 2D analysis of the [B] DEM reconstruction of the southern distal flow front emplaced during the 2022 Meradalir eruption. The pixel size for the analysis is 0.05 meters. The analysis reveals the directionality of the slabby pāhoehoe sheets.

al. 2016]. The Discrete Fourier Transform 2D analysis also reveals the ~E–W orientation as the direction of greatest variability at all spatial scales from ~5 to 30 m (Figure 12), which implies the dominant orientation of forces active during emplacement. Similar analysis can be applied to historic flows to improve interpretations of their emplacement dynamics.

The PyMTI-UAS instrument offers a contribution to future technological enhancement of multispectral TIR imaging system for volcanic and other geoscience applications. The development of a low-cost, versatile instrument that is deployable on multiple platforms (ground and air) to capture high-resolution TIR spectral data can provide new insights into dynamic geological processes. We demonstrate that it is possible to develop relatively inexpensive, operationally-flexible multispectral TIR imaging systems that can acquire accurate thermal and spectral information of volcanic process across a variety of temperatures. PyMTI-UAS has limitations and offers the potential for future development. For example, the lack of real-time data telemetry limits the application for rapid data analysis and hazard assessment, but this can be achieved through the integration of a data downlink. Another limitation relates to the optical design that limited the radiometric calibration. Future development could involve redesigning the optics with the filters between the lens and focal plane array, with the flat field correction shutter on the outer most optical surface. This would also reduce the geometric correction required. The spatial (~0.1 m) and temporal (1 Hz) resolution and field of view (8–22 m) also limited operating from close distances to maintain the high-resolution required to provide insightful science data and actionable analysis for hazard response. Sensors with larger focal plane arrays can be integrated with the architecture to improve the overall operational flexibility by increasing the spatial resolution and field of view, with an improved data interface increasing temporal resolution. All these potential future developments will improve the applicability and adaptability potential. However, these will add cost, weight, and power requirements that may ultimately reduce the utility and adoptability of a system. Overall, we think the PyMTI-UAS provides a foundation for future development in multiple directions that can be tailored to applications addressing particular needs across geosciences and hazard management.

5 Conclusions

The 2022 Meradalir effusive eruption in Iceland provided an opportunity to test the capabilities of the PyMTI-UAS instrument and allowed us to develop algorithms to enable broad use of the instrument in the community and beyond. The PyMTI-UAS performed well, offering insights into thermal and gas flux from volcanic cones and lava flows post-emplacement. The multispectral thermal infrared data contained 10–50 mm spatial registration error between bands with up to 3 m horizontal georeferencing error, enabling the precise location of thermal anomalies within the lava flow field. The resulting thermal data contained cumulative temperature and emissivity errors of <4 % that provided the accuracy needed to detect subtle changes in lava surface temperature and gas fluxes from fumaroles. PyMTI-UAS successfully deployed on a small UAV for 30-minute flights with moderate wind conditions and, overall, acquired actionable data.

The high resolution visible and multispectral thermal infrared data were used to analyze lava surface textures and

morphologies and suggest some emplacement processes. The spectral and temperature data were able to constrain major spectral variabilities, surface oxidation, and thermal anomalies, as well as volcanic thermal and gas emissions from diffuse and point sources. However, there are limits to the detection capabilities of multispectral thermal infrared data from UAVs due to resolution, power, and mass constraints. Further deployment at active volcanic systems and thorough ground truthing of data will improve the accuracy and reliability of data, which will lead to higher confidence in results. The scientific results and conclusions discussed here offer some insights into the types of questions we hope to answer moving forward.

Overall, PyMTI-UAS was developed as a relatively inexpensive multispectral TIR instrument designed to be deployable on a small UAVs to maximize logistical flexibility. We want PyMTI-UAS to be an accessible resource that aids scientists, volcano observatories, and hazard agencies across the global community. The methodology and results developed for PyMTI-UAS during the 2022 Meradalir campaign provides a framework for further development and innovation, with the aim of improving monitoring and analysis of volcanic systems at all scales. Our hope is that PyMTI-UAS or similar innovations will enhance measurement capabilities of all scientists and agencies responsible for the investigation and response to volcanic activity, and that applications may even extend beyond volcanology, into other geological and geographical studies.

Author Contributions

James O. Thompson: Conceptualization, Formal analysis, Investigation, Methodology, Software, Visualization, Writing - original draft, Writing - review & editing. **Emanuel Giovanini**: Formal analysis, Visualization, Writing - original draft. **Kenneth S. Befus**: Funding acquisition, Project administration, Writing - review & editing. **Edward W. Marshall**: Investigation, Methodology, Writing - review & editing. **Chelsea M. Allison**: Investigation, Writing - review & editing.

Acknowledgements

This research was supported by NASA grant: 80NSSC23K1544 (Thompson) Marshall was supported in part by the Icelandic Research Fund, grant no. 228933-052. We are grateful to the University of Iceland, National Commissioner of the Icelandic Police, and Department of Civil Protection and Emergency Management in Iceland for helping to facilitate the fieldwork. The authors would like to thank the anonymous reviewers and Editor (Mike James) for their insightful and constructive comments, which improved the quality of this work.

Data Availability

All data from this study are available fully, openly, and without restrictions. The TIR data from the PyMTI-UAS and thermal and visible 3D reconstructions are available from Texas Data Repository at https://dataverse.tdl.org/dataverse/Iceland2022 (https://doi.org/10.18738/T8/7REMSJ, https://doi.org/10.18738/T8/VCSCML). The code for calibrating and processing the TIR data is available on GitHub at: https://github.com/jthompson2710/PyMTI-UAS (https://doi.org/10.5281/zenodo.15395769).

Copyright Notice

References

Albadra, A., K. Wood, L. Berthoud, A. Calway, M. Watson, H. Thomas, T. Richardson, E. Liu, and G. Chigna (2020). "Determining the three-dimensional structure of a volcanic plume using Unoccupied Aerial System (UAS) imagery". *Journal of Volcanology and Geothermal Research* 407, page 106731. DOI: 10.1016/j.jvolgeores.2019.106731.

Andaru, R., J.-Y. Rau, D. K. Syahbana, A. S. Prayoga, and H. D. Purnamasari (2021). "The use of UAV remote sensing for observing lava dome emplacement and areas of potential lahar hazards: An example from the 2017–2019 eruption crisis at Mount Agung in Bali". *Journal of Volcanology and Geothermal Research* 415, page 107255. DOI: 10.1016/j.jvolgeores.2021.107255.

Avolio, M. V., G. M. Crisci, S. Di Gregorio, R. Rongo, W. Spataro, and G. A. Trunfio (2006). "SCIARA 2: An improved cellular automata model for lava flows and applications to the 2002 Etnean crisis". *Computers and Geosciences* 32(7), pages 876–889. DOI: 10.1016/j.cageo.2005.10.026.

Barsotti, S., M. M. Parks, M. A. Pfeffer, B. A. Óladóttir, T. Barnie, M. M. Titos, K. Jónsdóttir, G. B. M. Pedersen, Á. R. Hjartardóttir, G. Stefansdóttir, T. Johannsson, Þ. Arason, M. T. Gudmundsson, B. Oddsson, R. H. Þrastarson, B. G. Ófeigsson, K. Vogfjörd, H. Geirsson, T. Hjörvar, S. von Löwis, G. N. Petersen, and E. M. Sigurðsson (2023). "The eruption in Fagradalsfjall (2021, Iceland): how the operational monitoring and the volcanic hazard assessment contributed to its safe access". *Natural Hazards* 116(3), pages 3063–3092. DOI: 10.1007/s11069-022-05798-7.

Bilotta, G., A. Cappello, A. Hérault, A. Vicari, G. Russo, and C. Del Negro (2012). "Sensitivity analysis of the MAGFLOW Cellular Automaton model for lava flow simulation". *Environmental Modelling and Software* 35, pages 122–131. DOI: 10.1016/j.envsoft.2012.02.015.

Biren, J., A. Slodczyk, J. Andújar, L. del Campo, L. Cosson, H. Li, E. Veron, C. Genevois, S. Ory, and M. Aufaristama (2022). "High temperature spectral emissivity of glass and crystal-bearing basalts". *Journal of Volcanology and Geothermal Research* 430, page 107623. DOI: 10.1016/j.jvolgeores.2022.107623.

Boreham, F., K. Cashman, A. Rust, and Á. Höskuldsson (2018). "Linking lava flow morphology, water availability and rootless cone formation on the Younger Laxá Lava, NE Iceland".

Journal of Volcanology and Geothermal Research 364, pages 1–19. DOI: 10.1016/j.jvolgeores.2018.08.019.

Calvari, S. and H. Pinkerton (2004). "Birth, growth and morphologic evolution of the 'Laghetto' cinder cone during the 2001 Etna eruption". *Journal of Volcanology and Geothermal Research* 132(2–3), pages 225–239. DOI: 10.1016/s0377-0273(03)00347-0.

Caracciolo, A., E. W. Marshall, E. Bali, H. H. Merill, S. A. Halldórsson, S. Matthews, O. Sigmarsson, S. M. Johnson, G. H. Guðfinnsson, J. Gunnarsson Robin, A. A. Aden, and B. F. Pilicita Masabanda (2024). "The 2021-23 Fagradalsfjall fires: geochemical and petrological insights". *EGU 2024 Conference Abstracts*, page 9163. DOI: 10.5194/egusphere-egu24-9163.

Carr, B. B., A. B. Clarke, J. R. Arrowsmith, L. Vanderkluysen, and B. E. Dhanu (2019). "The emplacement of the active lava flow at Sinabung Volcano, Sumatra, Indonesia, documented by structure-from-motion photogrammetry". *Journal of Volcanology and Geothermal Research* 382, pages 164–172. DOI: 10.1016/j.jvolgeores.2018.02.004.

Carr, B. B., E. Lev, T. Sawi, K. A. Bennett, C. S. Edwards, S. A. Soule, S. Vallejo Vargas, and G. I. Marliyani (2021). "Mapping and classification of volcanic deposits using multi-sensor unoccupied aerial systems". *Remote Sensing of Environment* 264, page 112581. DOI: 10.1016/j.rse.2021.112581.

Cashman, K. V., C. Thornber, and J. P. Kauahikaua (1999). "Cooling and crystallization of lava in open channels, and the transition of Pāhoehoe Lava to 'A'ā". *Bulletin of Volcanology* 61(5), pages 306–323. DOI: 10.1007/s004450050299.

deGraffenried, R., J. Hammer, H. Dietterich, R. Perroy, M. Patrick, and T. Shea (2021). "Evaluating lava flow propagation models with a case study from the 2018 eruption of Kīlauea Volcano, Hawai'i". *Bulletin of Volcanology* 83(11), page 65. DOI: 10.1007/s00445-021-01492-x.

Del Negro, C., L. Fortuna, A. Herault, and A. Vicari (2007). "Simulations of the 2004 lava flow at Etna volcano using the magflow cellular automata model". *Bulletin of Volcanology* 70(7), pages 805–812. DOI: 10.1007/s00445-007-0168-8.

Dragoni, M. and A. Tallarico (1994). "The effect of crystallization on the rheology and dynamics of lava flows". *Journal of Volcanology and Geothermal Research* 59(3), pages 241–252. DOI: 10.1016/0377-0273(94)90098-1.

Etchells, T., L. Berthoud, A. Calway, M. Watson, and K. Wood (2022). "Simulation, image generation, and tomographic reconstruction of idealized volcanic plumes". *International Journal of Remote Sensing* 43(11), pages 4208–4232. DOI: 10.1080/01431161.2022.2107409.

Fitch, E. P. and S. A. Fagents (2020). "Characteristics of rootless cone tephra emplaced by high-energy lava–water explosions". *Bulletin of Volcanology* 82(8), page 62. DOI: 10.1007/s00445-020-01393-5.

FLIR Systems (2014). *User's Manual - FLIR Ax5 Series*. URL: https://support.flir.com/DocDownload/Assets/dl/t559770-en-us.pdf.

– (2018). *FLIR Lepton Engineering Datasheet*. URL: https://www.flir.com/developer/lepton-integration/lepton-tech-docs/.

Gillespie, A. R., T. Matsunaga, S. Rokugawa, and S. J. Hook (1996). "Temperature and emissivity separation from Advanced Spaceborne Thermal Emission and Reflection Radiometer (ASTER) images". *Infrared Spaceborne Remote Sensing IV*. Edited by M. S. Scholl and B. F. Andresen. Volume 2817. SPIE. DOI: 10.1117/12.255172.

Global Volcanism Program (2022). *Volcanoes of the World, v.4.3.4*. Edited by E. Venzke. DOI: 10.5479/si.GVP.VOTW5-2024.5.2.

Gregg, T. K. and J. H. Fink (2000). "A laboratory investigation into the effects of slope on lava flow morphology". *Journal of Volcanology and Geothermal Research* 96(3–4), pages 145–159. DOI: 10.1016/s0377-0273(99)00148-1.

Gunnarson, S. R., J. M. C. Belart, B. V. Óskarsson, M. T. Gudmundsson, T. Högnadóttir, G. B. M. Pedersen, T. Dürig, and V. Pinel (2023). "Automated processing of aerial imagery for geohazards monitoring: Results from Fagradalsfjall eruption, SW Iceland, August 2022". *Zenodo*. DOI: 10.5281/ZENODO.7871187. [Dataset].

Halldórsson, S. A., E. W. Marshall, A. Caracciolo, S. Matthews, E. Bali, M. B. Rasmussen, E. Ranta, J. G. Robin, G. H. Guðfinnsson, O. Sigmarsson, J. Maclennan, M. G. Jackson, M. J. Whitehouse, H. Jeon, Q. H. A. van der Meer, G. K. Mibei, M. H. Kalliokoski, M. M. Repczynska, R. H. Rúnarsdóttir, G. Sigurðsson, M. A. Pfeffer, S. W. Scott, R. Kjartansdóttir, B. I. Kleine, C. Oppenheimer, A. Aiuppa, E. Ilyinskaya, M. Bitetto, G. Giudice, and A. Stefánsson (2022). "Rapid shifting of a deep magmatic source at Fagradalsfjall volcano, Iceland". *Nature* 609(7927), pages 529–534. DOI: 10.1038/s41586-022-04981-x.

Harris, A. J. L., L. P. Flynn, L. Keszthelyi, P. J. Mouginis-Mark, S. K. Rowland, and J. A. Resing (1998). "Calculation of lava effusion rates from Landsat TM data". *Bulletin of Volcanology* 60(1), pages 52–71. DOI: 10.1007/s004450050216.

Harris, A. J. L. and S. K. Rowland (2001). "FLOWGO: a kinematic thermo-rheological model for lava flowing in a channel". *Bulletin of Volcanology* 63(1), pages 20–44. DOI: 10.1007/s004450000120.

Harris, A. J. L., S. K. Rowland, N. Villeneuve, and T. Thordarson (2016). "Pāhoehoe, 'a'ā, and block lava: an illustrated history of the nomenclature". *Bulletin of Volcanology* 79(1), page 7. DOI: 10.1007/s00445-016-1075-7.

Head, J. W. and L. Wilson (1989). "Basaltic pyroclastic eruptions: Influence of gas-release patterns and volume fluxes on fountain structure, and the formation of cinder cones, spatter cones, rootless flows, lava ponds and lava flows". *Journal of Volcanology and Geothermal Research* 37(3–4), pages 261–271. DOI: 10.1016/0377-0273(89)90083-8.

Hennig, B. (2023). *Where the lava flows: Volcano update from Iceland*. Accessed: 2024-08-01. URL: https://www.viewsoftheworld.net/?p=5783.

Herault, A., A. Vicari, A. Ciraudo, and C. Del Negro (2009). "Forecasting lava flow hazards during the 2006 Etna eruption: Using the MAGFLOW cellular automata model". *Com-*

puters and Geosciences 35(5), pages 1050–1060. DOI: 10.1016/j.cageo.2007.10.008.

Hutchison, W., N. Varley, D. M. Pyle, T. A. Mather, and J. A. Stevenson (2013). "Airborne thermal remote sensing of the Volcán de Colima (Mexico) lava dome from 2007 to 2010". *Geological Society, London, Special Publications* 380(1), pages 203–228. DOI: 10.1144/sp380.8.

James, M. R., B. Carr, F. D'Arcy, A. Diefenbach, H. Dietterich, A. Fornaciai, E. Lev, E. Liu, D. Pieri, M. Rodgers, B. Smets, A. Terada, F. Von Aulock, T. Walter, K. Wood, and E. Zorn (2020). "Volcanological applications of unoccupied aircraft systems (UAS): Developments, strategies, and future challenges". *Volcanica* 3(1), pages 67–114. DOI: 10.30909/vol.03.01.67114.

Kahl, M., E. Mutch, J. Maclennan, D. Morgan, F. Couperthwaite, E. Bali, T. Thordarson, G. Guðfinnsson, R. Walshaw, I. Buisman, S. Buhre, Q. van der Meer, A. Caracciolo, E. W. Marshall, M. Rasmussen, C. Gallagher, W. Moreland, Á. Höskuldsson, and R. Askew (2022). "Deep magma mobilization years before the 2021 CE Fagradalsfjall eruption, Iceland". *Geology* 51(2), pages 184–188. DOI: 10.1130/g50340.1.

Kósik, S., K. Németh, G. Kereszturi, J. Procter, G. Zellmer, and N. Geshi (2016). "Phreatomagmatic and water-influenced Strombolian eruptions of a small-volume parasitic cone complex on the southern ringplain of Mt. Ruapehu, New Zealand: Facies architecture and eruption mechanisms of the Ohakune Volcanic Complex controlled by an unstable fissure eruption". *Journal of Volcanology and Geothermal Research* 327, pages 99–115. DOI: 10.1016/j.jvolgeores.2016.07.005.

Liu, R., H. Zhang, and S. Scherer (2023). *Multiple methods of geometric calibration of thermal camera and a method of extracting thermal calibration feature points*. URL: https://henryzh47.github.io/assets/documents/multiple-methods-geometric.pdf.

Lowenstern, J. B., K. Wallace, S. Barsotti, L. Sandri, W. Stovall, B. Bernard, E. Privitera, J.-C. Komorowski, N. Fournier, C. Balagizi, and E. Garaebiti (2022). "Guidelines for volcano-observatory operations during crises: recommendations from the 2019 volcano observatory best practices meeting". *Journal of Applied Volcanology* 11(1), page 3. DOI: 10.1186/s13617-021-00112-9.

Marshall, E. W., A. Caracciolo, E. Bali, S. A. Halldórsson, S. Matthews, E. Ranta, M. B. Rasmussen, J. G. Robin, G. H. Guðfinnson, J. Maclennan, C. Bosq, D. Auclair, O. Sigmarsson, H. Merrill, B. Gísladóttir, S. Johnson, N. Löw, A. Stracke, and F. Genske (2024). "The Petrology and Geochemistry of the 2021 Fagradalsfjall Eruption, Iceland: An Eruption Sourced From Multiple, Compositionally Diverse, Near-Moho Sills". *AGU Advances* 5(6), e2024AV001310. DOI: 10.1029/2024av001310.

Marshall, E. W., A. Caracciolo, E. Ranta, E. Bali, S. Halldorsson, J. Gunnarsson-Robin, O. Sigmarsson, M. Bar Rasmussen, G. Guðfinnsson, S. Matthews, and N. Lowe (2023). "Geochemical evolution of the 2021 and 2022 Fagradalsfjall eruptions". *Goldschmidt 2023 Conference Abstracts*. DOI: 10.7185/gold2023.18545.

Matthews, S. W., A. Caracciolo, E. Bali, S. A. Halldórsson, O. Sigmarsson, G. H. Guðfinnsson, G. B. M. Pedersen, J. G. Robin, E. W. Marshall, A. A. Aden, B. Ý. Gísladóttir, C. Bosq, D. Auclair, H. Merrill, N. Levillayer, N. Löw, R. H. Rúnarsdóttir, S. M. Johnson, S. Steinþórsson, and V. Drouin (2024). "A dynamic mid-crustal magma domain revealed by the 2023 to 2024 Sundhnúksgígar eruptions in Iceland". *Science* 386(6719), pages 309–314. DOI: 10.1126/science.adp8778.

Matungka, R., Y. F. Zheng, and R. L. Ewing (2008). "Image registration using Adaptive Polar Transform". *2008 15th IEEE International Conference on Image Processing*. IEEE, pages 2416–2419. DOI: 10.1109/icip.2008.4712280.

Park, S. and J. D. Iversen (1984). "Dynamics of lava flow: Thickness growth characteristics of steady two-dimensional flow". *Geophysical Research Letters* 11(7), pages 641–644. DOI: 10.1029/gl011i007p00641.

Parks, M. M., F. Sigmundsson, V. Drouin, Á. R. Hjartardóttir, H. Geirsson, A. Hooper, K. S. Vogfjörd, B. G. Ófeigsson, S. Hreinsdóttir, E. H. Jensen, P. Einarsson, S. Barsotti, and H. M. Fridriksdóttir (2023). "Deformation, seismicity, and monitoring response preceding and during the 2022 Fagradalsfjall eruption, Iceland". *Bulletin of Volcanology* 85(10), page 60. DOI: 10.1007/s00445-023-01671-y.

Parks, M. M., F. Sigmundsson, V. Drouin, S. Hreinsdóttir, A. Hooper, Y. Yang, B. G. Ófeigsson, E. Sturkell, Á. R. Hjartardóttir, R. Grapenthin, H. Geirsson, E. Trasatti, S. Barsotti, R. Pedersen, P. Einarsson, B. A. Óladóttir, and H. M. Friðriksdóttir (2024). "2021–2023 Unrest and Geodetic Observations at Askja Volcano, Iceland". *Geophysical Research Letters* 51(4), e2023GL106730. DOI: 10.1029/2023gl106730.

Pedersen, G. B. M., J. M. C. Belart, B. V. Óskarsson, S. R. Gunnarson, M. T. Gudmundsson, H. I. Reynolds, G. Valsson, T. Högnadóttir, V. Pinel, M. M. Parks, V. Drouin, R. A. Askew, T. Dürig, and R. H. Þrastarson (2024). "Volume, effusion rates and lava hazards of the 2021, 2022 and 2023 Reykjanes fires: Lessons learned from near real-time photogrammetric monitoring". *EGU 2024 Conference Abstracts*, page 10724. DOI: 10.5194/egusphere-egu24-10724.

Pedersen, G. B. M., J. M. C. Belart, B. V. Óskarsson, M. T. Gudmundsson, N. Gies, T. Högnadóttir, Á. R. Hjartardóttir, V. Pinel, E. Berthier, T. Dürig, H. I. Reynolds, C. W. Hamilton, G. Valsson, P. Einarsson, D. Ben-Yehosua, A. Gunnarsson, and B. Oddsson (2022). "Volume, Effusion Rate, and Lava Transport During the 2021 Fagradalsfjall Eruption: Results From Near Real-Time Photogrammetric Monitoring". *Geophysical Research Letters* 49(13), e2021GL097125. DOI: 10.1029/2021gl097125.

Pulido, C. M. and N. R. Riggs (2013). "Processes during scoria-cone collapse as recorded by displacement of crater-rim blocks, Strawberry Crater, AZ". *Geology of Route 66 Region: Flagstaff to Grants*. New Mexico Geological Society, pages 153–158. DOI: 10.56577/ffc-64.153.

Ramsey, M. S. and A. J. L. Harris (2013). "Volcanology 2020: How will thermal remote sensing of volcanic surface activity evolve over the next decade?" *Journal of Volcanology and Geothermal Research* 249, pages 217–233. DOI: 10.1016/j.jvolgeores.2012.05.011.

Ramsey, M. S., A. J. L. Harris, and I. M. Watson (2022). "Volcanology 2030: will an orbital volcano observatory finally become a reality?" *Bulletin of Volcanology* 84(1), page 6. DOI: 10.1007/s00445-021-01501-z.

Reddy, B. and B. Chatterji (1996). "An FFT-based technique for translation, rotation, and scale-invariant image registration". *IEEE Transactions on Image Processing* 5(8), pages 1266–1271. DOI: 10.1109/83.506761.

Reynolds, P., R. J. Brown, T. Thordarson, E. W. Llewellin, and K. Fielding (2015). "Rootless cone eruption processes informed by dissected tephra deposits and conduits". *Bulletin of Volcanology* 77(9), page 72. DOI: 10.1007/s00445-015-0958-3.

Roshan, M. C., M. Isaksson, and A. Pranata (2024). "A geometric calibration method for thermal cameras using a ChArUco board". *Infrared Physics and Technology* 138, page 105219. DOI: 10.1016/j.infrared.2024.105219.

Rothman, L., I. Gordon, Y. Babikov, A. Barbe, D. Chris Benner, P. Bernath, M. Birk, L. Bizzocchi, V. Boudon, L. Brown, A. Campargue, K. Chance, E. Cohen, L. Coudert, V. Devi, B. Drouin, A. Fayt, J.-M. Flaud, R. Gamache, J. Harrison, J.-M. Hartmann, C. Hill, J. Hodges, D. Jacquemart, A. Jolly, J. Lamouroux, R. Le Roy, G. Li, D. Long, O. Lyulin, C. Mackie, S. Massie, S. Mikhailenko, H. Müller, O. Naumenko, A. Nikitin, J. Orphal, V. Perevalov, A. Perrin, E. Polovtseva, C. Richard, M. Smith, E. Starikova, K. Sung, S. Tashkun, J. Tennyson, G. Toon, V. Tyuterev, and G. Wagner (2013). "The HITRAN2012 molecular spectroscopic database". *Journal of Quantitative Spectroscopy and Radiative Transfer* 130, pages 4–50. DOI: 10.1016/j.jqsrt.2013.07.002.

Sæmundsson, K., M. Á. Sigurgeirsson, and G. Ó. Friðleifsson (2020). "Geology and structure of the Reykjanes volcanic system, Iceland". *Journal of Volcanology and Geothermal Research* 391, page 106501. DOI: 10.1016/j.jvolgeores.2018.11.022.

Soldati, A., D. B. Dingwell, T. Thordarson, Á. Höskuldsson, I. Jónsdóttir, W. M. Moreland, J. S. Pálmadóttir, C. R. Gallagher, H. K. Torfadóttir, J. G. Licari, I. K. Valdimarsdóttir, L. B. Pétursdóttir, and R. A. Askew (2024). "A lower bound on the rheological evolution of magma in the 2021 Fagradalsfjall Fires". *Journal of Volcanology and Geothermal Research* 451, page 108098. DOI: 10.1016/j.jvolgeores.2024.108098.

Spampinato, L., S. Calvari, C. Oppenheimer, and E. Boschi (2011). "Volcano surveillance using infrared cameras". *Earth-Science Reviews* 106(1–2), pages 63–91. DOI: 10.1016/j.earscirev.2011.01.003.

Tang, Y., D. Q. Tong, K. Yang, P. Lee, B. Baker, A. Crawford, W. Luke, A. Stein, P. C. Campbell, A. Ring, J. Flynn, Y. Wang, J. McQueen, L. Pan, J. Huang, and I. Stajner (2020). "Air quality impacts of the 2018 Mt. Kilauea Volcano eruption in Hawaii: A regional chemical transport model study with satellite-constrained emissions". *Atmospheric Environment* 237, page 117648. DOI: 10.1016/j.atmosenv.2020.117648.

Thompson, J. O. and M. S. Ramsey (2020a). "Spatiotemporal variability of active lava surface radiative properties using ground-based multispectral thermal infrared data". *Journal of Volcanology and Geothermal Research* 408, page 107077. DOI: 10.1016/j.jvolgeores.2020.107077.

– (2020b). "Uncertainty Analysis of Remotely-Acquired Thermal Infrared Data to Extract the Thermal Properties of Active Lava Surfaces". *Remote Sensing* 12(1), page 193. DOI: 10.3390/rs12010193.

Thompson, J. O., M. S. Ramsey, and J. L. Hall (2019). "MMT-Cam: A New Miniature Multispectral Thermal Infrared Camera System for Capturing Dynamic Earth Processes". *IEEE Transactions on Geoscience and Remote Sensing* 57(10), pages 7438–7446. DOI: 10.1109/tgrs.2019.2913344.

Thordarson, T. and S. Self (1998). "The Roza Member, Columbia River Basalt Group: A gigantic pahoehoe lava flow field formed by endogenous processes?" *Journal of Geophysical Research: Solid Earth* 103(B11), pages 27411–27445. DOI: 10.1029/98jb01355.

Valentine, G. A., D. J. Krier, F. V. Perry, and G. Heiken (2007). "Eruptive and geomorphic processes at the Lathrop Wells scoria cone volcano". *Journal of Volcanology and Geothermal Research* 161(1–2), pages 57–80. DOI: 10.1016/j.jvolgeores.2006.11.003.

Vicari, A., G. Ganci, B. Behncke, A. Cappello, M. Neri, and C. Del Negro (2011). "Near-real-time forecasting of lava flow hazards during the 12-13 January 2011 Etna eruption: forecasting of lava flow hazards at Etna". *Geophysical Research Letters* 38(13), page L13317. DOI: 10.1029/2011gl047545.

Vicari, A., A. Ciraudo, C. Del Negro, A. Herault, and L. Fortuna (2008). "Lava flow simulations using discharge rates from thermal infrared satellite imagery during the 2006 Etna eruption". *Natural Hazards* 50(3), pages 539–550. DOI: 10.1007/s11069-008-9306-7.

Volcanology and Natural Hazards Research Group (2022). *DO NOT WALK ON THE LAVA! Old or New.* URL: https://www.facebook.com/Natturuva/posts/pfbid02XrYSHXeorztsMPCquE3xSx98AdnHtJjG6vA41CZwbZcrpDP3w2LHDrkmbYQNGW8sl.

Wainman, L., E. Ilyinskaya, M. Pfeffer, C. Mandon, E. Bali, B. A. Edwards, B. I. Kleine-Marshall, S. R. Gudjonsdottir, A. Cotterill, S. W. Scott, P. Wieser, A. Stefánsson, E. J. Nicholson, J. Sepulveda-Araya, S. J. Hammond, B. E. Kunz, F. Jenner, J. R. Gunnarsson, A. Aiuppa, M. Burton, and T. A. Mather (2024). "Trace Element Emissions Vary With Lava Flow Age and Thermal Evolution During the Fagradalsfjall 2021–2023 Eruptions, Iceland". *Geochemistry, Geophysics, Geosystems* 25(12), e2024GC011822. DOI: 10.1029/2024gc011822.

Xie, H., N. Hicks, G. Randy Keller, H. Huang, and V. Kreinovich (2003). "An IDL/ENVI implementation of the FFT-based algorithm for automatic image registration". *Computers and Geosciences* 29(8), pages 1045–1055. DOI: 10.1016/s0098-3004(03)00104-3.

Zhang, Z. (2000). "A flexible new technique for camera calibration". *IEEE Transactions on Pattern Analysis and Machine Intelligence* 22(11), pages 1330–1334. DOI: 10.1109/34.888718.